Euler Procedure for Correcting Two-Dimensional Transonic Wind-Tunnel Wall Interference

Magdi H. Rizk* and Donald R. Lovell†
Flow Research Company, Kent, Washington
and
Timothy J. Baker‡
Princeton University, Princeton, New Jersey

Based on an optimization formulation, a procedure has been developed to evaluate Mach number and angle-of-attack corrections. The Euler equations are assumed to be the flow governing equations. To obtain efficient solutions for the optimization problem, the iterative solutions for the flow variables and the design parameters are simultaneously updated. This is done by using a scheme that eliminates the limitations of a previously developed scheme. In addition to the model lift and geometry, the procedure requires pressure measurements near the tunnel walls. The accuracy and efficiency of several optimization techniques are investigated. The effect of perturbing certain test conditions on the residual interference is investigated.

Introduction

AIRCRAFT models are tested in wind tunnels to study their aerodynamic properties and to estimate their performance qualities. Because of wall interference effects, however, the properties observed in the wind tunnel differ from those observed under free-air conditions. To estimate correctly the free-air performance of the tested models and to achieve the maximum benefit from wind-tunnel tests for design improvements, it is necessary to determine the wall interference effects and to correct for them accurately.

The classical procedure[1] for correcting wall interference effects is based on linear theory. Although it provides insight into the features of wall interference, it does not produce sufficiently accurate formulas for practical use. A major source of error in the classical approach has been eliminated by wall interference correction procedures that replace the inaccurate homogeneous wall boundary conditions with measured flow properties. Procedures that require pressure measurements along a contour neighboring the tunnel walls,[2] measurements of a single flow quantity along two contours,[3] and measurements of two flow variables at a single contour[4] have been developed. These and other methods summarized in Ref. 5 are applicable to linear, subsonic flows. Two-dimensional transonic wall interference correction procedures have been developed by Kemp[6,7] and Murman.[8] These procedures use measured pressures near the tunnel walls and on the model surface. Solutions of the transonic small-disturbance equations are obtained and used to determine Mach number and angle-of-attack corrections.

The two-dimensional correction procedure presented here is formulated as an optimization problem. The Euler equations are assumed to be the flow governing equations, and the limitations of using the small-disturbance assumption are removed. Body-fitted coordinates are used to apply accurately the surface boundary conditions. The three-dimensional transonic correction procedure developed in Ref. 9 includes a number of simplifying assumptions that need to be replaced by more accurate formulations to allow the prediction of wall interference effects for real test models. An extension of the present two-dimensional method to three-dimensional configurations would satisfy this need.

Received July 20, 1987; revision received Feb. 12, 1988.

*Senior Research Scientist. Member AIAA.
†Scientific Programmer.
‡Research Scientist. Member AIAA.

Formulation

Flow Governing Equations

The correction procedure is divided into two basic steps. In the first and second steps, the flow is numerically simulated about the airfoil in the wind tunnel and in free air, respectively. The Euler equations

$$\mathbf{D}(\mathbf{W};M_\infty) \equiv \frac{\partial}{\partial x}\mathbf{f}(\mathbf{W};M_\infty) + \frac{\partial}{\partial y}\mathbf{g}(\mathbf{W};M_\infty) = 0 \qquad (1)$$

are assumed to be the flow governing equations, where

$$\mathbf{W} = \begin{bmatrix} \rho \\ \rho u \\ \rho v \\ \rho E \end{bmatrix}, \quad \mathbf{f} = \begin{bmatrix} \rho u M_\infty \\ \rho u^2 M_\infty^2 + (p/\gamma) \\ \rho u v M_\infty^2 \\ \rho u H M_\infty \end{bmatrix}, \quad \mathbf{g} = \begin{bmatrix} \rho v M_\infty \\ \rho v u M_\infty^2 \\ \rho v^2 M_\infty^2 + (p/\gamma) \\ \rho v H M_\infty \end{bmatrix} \qquad (2)$$

ρ, a, and p are the density, speed of sound, and pressure, respectively, normalized by their respective freestream values; u and v are the Cartesian velocity components normalized by the freestream velocity; x and y are the Cartesian coordinates; and γ is the ratio of specific heats. The total energy E and total enthalpy H normalized by the square of the freestream speed of sound are given by

$$H = E + (p/\gamma\rho)$$

$$E = [p/\gamma(\gamma - 1)\rho] + \tfrac{1}{2}M_\infty^2(u^2 + v^2)$$

where $p = \rho a^2$. The normalization used here allows the freestream Mach number M_∞ to appear explicitly in the governing equations. This explicit appearance is a requirement of the correction scheme.

Outer Boundary Conditions for Wind Tunnel Simulation

Following Ref. 10, the treatment of the tunnel boundary conditions, in the first step of the correction procedure, and the free air far-field boundary conditions, in the second step of the correction procedure, are based on the introduction of the Riemann invariants for a one-dimensional flow normal to the boundary. The free air far-field boundary conditions used here are given in Ref. 10.

In the first step of the correction procedure, the system of equations, Eq. (1), is solved subject to an experimentally measured pressure distribution on the horizontal boundaries of a rectangle and to appropriate boundary conditions (either experimental or theoretical) on the vertical boundaries of the rectangle. The sides of the rectangle are assumed to be close to the tunnel walls but outside the boundary-layer region. It is this rectangle that defines the boundaries of the computational domain for the tunnel simulation.

Boundary conditions at the vertical boundaries of the computational domain, based on experimental measurements, were derived in Ref. 11. Using present experimental techniques, it is not practical to obtain experimental measurements at the upstream and downstream boundaries. In the present work, boundary conditions similar to those of the far field in free air are applied at the upstream and the downstream boundaries.

At the upper and lower boundaries, the Riemann invariant corresponding to the outgoing characteristic introduces the following relation between q_{nB} and a_B:

$$R_B \equiv M_\infty q_{nB} + [2/(\gamma-1)]a_B = R_E \equiv M_\infty q_{nE} + [2/(\gamma-1)]a_E \quad (3)$$

where q_n is the velocity component normal to the boundary and pointing outward and the subscripts B and E denote the boundary and the interior computational cells adjacent to the boundary, respectively.

The use of Eq. (3) for two-dimensional flows is an approximation. In these flows, R_B and R_E are related at steady state by

$$R_B = R_E + [(n_B - n_E)G/(q_n + a)] \quad (4)$$

where

$$G = -M_\infty^2 q_\tau \frac{\partial}{\partial \tau} q_n - \frac{a}{\rho}\frac{\partial}{\partial \tau}(pq_\tau)M_\infty$$

and where q_τ is the velocity component tangent to the boundary, τ is the coordinate in the direction of the boundary, and n is the coordinate normal to the boundary. The error introduced by using Eq. (3) instead of Eq. (4) is given by the last term in Eq. (4). This error is expected to be small provided that the derivatives of the solution along the boundary are small and provided that the distance between the boundary and the center of the adjacent mesh cells is small.

The normal velocity component q_{nB} is evaluated from Eq. (3) with

$$a_B = (p_B/\rho_E)^{1/2}(p_E/p_B)^{1/2\gamma} \quad (5)$$

The equation for the total enthalpy is then used to evaluate $q_{\tau B}$, which is given by

$$q_{\tau B} = \sqrt{(2/M_\infty^2)\{H_\infty - [1/(\gamma-1)]a_B^2\} - q_{nB}^2} \quad (6)$$

The total energy is evaluated by the relation

$$E_B = H_\infty - (a_B^2/\gamma) \quad (7)$$

Correction Procedure

In the first step of the correction procedure, an equivalent angle of attack α_T is determined such that the tunnel-computed lift coefficient L_T matches the measured lift coefficient L_e of the tested model, where the subscript T denotes computed tunnel conditions and the subscript e denotes experimental conditions. Let $\mathbf{P}_T$ denote the parameters α_T and $M_{\infty T}$. The problem solved in this step may be stated as follows. Find α_T subject to the constraint

$$E_L(\mathbf{P}_T;\mathbf{W}_T) \equiv \{[L_T(\mathbf{P}_T;\mathbf{W}_T) - L_e]/L_e\} = 0 \quad (8a)$$

with $\mathbf{W}_T$ satisfying the equation

$$\mathbf{D}(\mathbf{W}_T;M_{\infty T}) = 0 \quad (8b)$$

Although α_T, the first component of $\mathbf{P}_T$, is determined in this step, the second component $M_{\infty T}$ is set equal to the measured value $M_{\infty e}$.

In the second step of the correction procedure, the free-air flow is numerically simulated. The free-air angle of attack α_F and Mach number $M_{\infty F}$ are determined in this step. Let $\boldsymbol{P}_F$ denote the parameters α_F and $M_{\infty F}$. The problem solved is an optimization problem in which $\boldsymbol{P}_F$ is the vector of design parameters. The optimum value of $\boldsymbol{P}_F$, $\boldsymbol{P}_F^*$ is determined such that the objective function E_M satisfies the condition

$$E_M(\mathbf{P}_F^*;\mathbf{W}_F) = \min_{\mathbf{P}_F} E_M(\mathbf{P}_F;\mathbf{W}_F) \quad (9a)$$

subject to the constraint

$$E_\alpha(\mathbf{P}_F;\mathbf{W}_F) \equiv \frac{\eta L_F(\mathbf{P}_F;\mathbf{W}_F) - L_T(\mathbf{P}_T;\mathbf{W}_T)}{L_T(\mathbf{P}_T;\mathbf{W}_T)} = 0 \quad (9b)$$

with $\mathbf{W}_F$ satisfying the equation

$$\mathbf{D}(\mathbf{W}_F;M_{\infty F}) = 0 \quad (9c)$$

Here the subscript F denotes computed free-air conditions. The objective function E_M, which is minimized in the problem, is given by

$$E_M \equiv \frac{\int (M_F - M_T)^2\, ds}{\int M_T^2\, ds} \quad (10)$$

This is a measure of the Mach number difference on the model surface in the tunnel and in free air. The integrals are taken over the model surface. In Eq. (9b), L_F is the free-air-calculated lift coefficient. Two formulations are considered here. In the first formulation, η in Eq. (9b) is given by

$$\eta = 1 \quad (11a)$$

In this case, the free-air-computed lift coefficient is constrained to the value of the wind-tunnel lift coefficient. In the second formulation, η in Eq. (9b) is given by

$$\eta = [\xi(M_{\infty F})/\xi(M_{\infty T})] \quad (11b)$$

where

$$\xi(M_\infty) = \left[\tfrac{1}{2}\gamma M_\infty^2 \Big/ \left(1 + \frac{\gamma-1}{2}M_\infty^2\right)^{\gamma/\gamma-1}\right]$$

is the ratio of the freestream dynamic pressure to the freestream total pressure. In this case, the lift coefficients used in the first formulation are replaced by modified lift coefficients in which the freestream total pressure replaces the freestream dynamic pressure for the normalization of the lift. The regular definition of the lift coefficient has an explicit dependence on the freestream Mach number. The modified definition of the lift coefficient removes this dependence, and therefore it is more suitable.

The Mach number and angle-of-attack corrections are calculated from the relations

$$\Delta M = M_{\infty F} - M_{\infty T}, \qquad \Delta\alpha = \alpha_F - \alpha_T \tag{12}$$

and the corrected Mach number and angle of attack are then found from the relations

$$M_{\infty f} = M_{\infty e} + \Delta M, \qquad \alpha_f = \alpha_e + \Delta\alpha \tag{13}$$

where the subscript f is used to denote the corrected conditions.

Numerical Approach

The objective of the correction procedure is to determine the parameters α_T, α_F, and $M_{\infty F}$. To determine these parameters, it is necessary to determine the flow solution $\mathbf{W}$. The procedure for obtaining the solution $\mathbf{W}$ for the Euler equations in a regular analysis problem is an iterative procedure in which $\mathbf{W}$ is repeatedly updated until convergence is achieved. The approach used here follows that used in determining the analysis problem solution with the exception of allowing the parameters α_T, α_F, and $M_{\infty F}$ to be updated as $\mathbf{W}$ is updated so that convergence is achieved for the flow solution and the parameters α_T, α_F, and $M_{\infty F}$ simultaneously. The flow solver is based on a finite-volume discretization and uses a multigrid strategy together with a multistage time-stepping scheme to advance the flow solution to a steady state as rapidly as possible. Details of the dissipative terms, the multistage schemes, and the multigrid method are given in Refs. 10, 12, and 13. A description of the mesh used in the computations follows.

Mesh Generation

An H-type mesh is generated in order to allow the mesh lines to coincide with the wind-tunnel wall, as well as the airfoil surface. Define a complex variable $z = x + iy$, and let z_0 represent a singular point located just inside the airfoil leading edge. We now define a new complex variable $Z = X + iY$, corresponding to a point (X,Y) in mapped space. Setting $z - z_0 = re^{i\theta}$, the mapping

$$Z = kf(r)e^{i\theta/2} \tag{14}$$

is applied to the airfoil surface, with $f(r) = r^{1/2}$, where k is a constant scaling factor. The mapping given by Eq. (14) is also applied to a Cartesian mesh in physical space, with stretching in the x and y directions to cluster points near the airfoil, with

$$f(r) = (r/\sqrt{r} + \varepsilon)$$

This variable scaling has the effect of pulling points close to the origin in the mapped space.[14] It leads to a concentration of mesh points close to the airfoil leading edge. We now deform the mesh lines in mapped space so that the X axis is displaced to coincide with the airfoil surface. Thus, if $S(X)$ represents the airfoil shape in mapped space, we apply a shearing transformation to all mesh points. We then invert the square root mapping procedure to obtain the conforming H mesh in physical space

$$z' = z_0 + (1/k^2)Z'^2 \tag{15}$$

where

$$Z' = X + i\,[Y + S(X)]$$

Although the free-air computational mesh does not require that its outer boundary mesh lines conform to a specific shape, the wind-tunnel computational mesh requires that they be straight. Mesh shearing is therefore applied in the physical plane to achieve this requirement. The mesh spacing requirements for a free-air mesh and a tunnel mesh differ. The free-air solution has its largest gradients near the airfoil surface, requiring a relatively fine mesh there. As one moves away from the airfoil, these gradients diminish. A computational mesh that is increasingly stretched as the outer boundaries are approached is therefore appropriate for free-air computations. In the tunnel, the flow solution near the airfoil has mesh requirements similar to those in free air. However, the solution as the tunnel boundary is approached is expected to have higher mesh resolution requirements than that of free air, due to the tunnel constraint. It is essential to have equivalent computational meshes in the tunnel and in free air at both the model surface and in the region surrounding the model surface, where the two solutions are expected to be close, to minimize relative truncation effects. The free-air mesh can be chosen to coincide with the tunnel mesh in their overlapping region; however, increased computational efficiency can be achieved by having the two meshes deviate as the tunnel boundary position is approached, since resolution requirements for free-air computations are lower than those for wind-tunnel computations there.

Correction Scheme

Step 1: Wind-Tunnel Simulation

The goal in this step is to determine the value of the airfoil angle of attack α_T that causes the airfoil-computed lift coefficient L_T to be equal to the experimental value L_e. In this step, a solution for the wind-tunnel flowfield is obtained. The flow-field solution is obtained iteratively in a manner similar to that used for solving an analysis problem, with the exception of allowing α_T to vary as the computation progresses. Prior to the $(n+1)$th iterative step, in which the flow solution is updated, α_T is updated so that the value used in this step is α_T^{n+1},

$$\alpha_T^{n+1} = \alpha_T^n + \delta\alpha_T^{n+1} \tag{16}$$

The increment $\delta\alpha_T^{n+1}$ is determined by the chord method and is given by

$$\delta\alpha_T^{n+1} = -\frac{E_L^n}{|E_L^n|}\,[\min(C_\alpha|E_L^n|, A_\alpha)] \tag{17}$$

where

$$E_L^n = E_L(\alpha_T^n, M_{\infty T}; \mathbf{W}_T^n)$$

and A_α and C_α are positive constants. The constant A_α sets an upper limit on the magnitude of $\delta\alpha_T^{n+1}$.

Step 2: Free-Air Simulation

The goal in this step is to determine the values for the airfoil angle of attack α_F and the free-air Mach number $M_{\infty F}$ that minimize the objective function E_M subject to the lift constraint given in Eq. (9b). A search must therefore be conducted in the design parameter space α_F and $M_{\infty F}$ for the optimum solution. This optimization problem is most conveniently solved in the rotated design parameter space α'_F and $M'_{\infty F}$ with the α'_F coordinate normal to the constant-lift constraint and the $M'_{\infty F}$ coordinate parallel to the constraint. For fixed values of α'_F and $M'_{\infty F}$, let

$$\mathbf{W}_F^{n+1} = \psi(\mathbf{W}_F^n, \alpha'_F, M'_{\infty F}), \qquad n = 0,1,2,\ldots \tag{18}$$

be the iterative solution for the analysis problem, where ψ denotes the solution obtained by applying the iterative (time-stepping) scheme for solving the Euler equations once using $\mathbf{W}_F^n$ as an initial guess. As for the analysis solution, obtaining the optimization solution requires the repeated application of Eq. (18) to update the flowfield. Although α'_F and $M'_{\infty F}$ are held fixed in the former case, they are allowed to vary in the latter. The scheme used to update these parameters follows.

The values of α'_F and $M'_{\infty F}$ are updated every ΔN iterations. Therefore,

$$\alpha'^{n+1}_F = \alpha'^{n}_F + \delta\alpha'^{n+1}_F \tag{19a}$$

$$M'^{n+1}_{\infty F} = M'^{n}_{\infty F} + \delta M'^{n+1}_{\infty F} \tag{19b}$$

where

$$\delta\alpha'^{n+1}_F = 0, \qquad (n+1)/\Delta N \neq 1,2,3,...$$

$$\delta M'^{n+1}_{\infty F} = 0, \qquad (n+1)/\Delta N \neq 1,2,3,...$$

In the iterative steps that satisfy the relation $(n+1)/\Delta N = 1,2,3,...$, the incremental values for the design parameters are given by

$$\delta\alpha'^{n+1}_F = -\frac{E^n_\alpha}{|E^n_\alpha|}[\min(C_\alpha|E^n_\alpha|, A_\alpha)] \tag{20a}$$

$$\delta M'^{n+1}_{\infty F} = \tfrac{1}{2}[c_1(\tau^{n+1}+1) + c_2(\tau^{n+1}-1)]\delta M'^{n+1-\Delta N}_{\infty F} \tag{20b}$$

where

$$E^n_\alpha = E_\alpha(\mathbf{P}^n_F; \mathbf{W}^n_F) \tag{21}$$

$$\tau^{n+1} = -\frac{\Delta E^n_M \delta M'^{n+1-\Delta N}_{\infty F}}{|\Delta E^n_M \delta M'^{n+1-\Delta N}_{\infty F}|} \tag{22}$$

$$\Delta E^n_M = E_M(\alpha'^{n}_F, M'^{n}_{\infty F} + \varepsilon; \mathbf{W}^n_{F,\varepsilon}) - E_M(\alpha'^{n}_F, M'^{n}_{\infty F}; \mathbf{W}^n_F) \tag{23}$$

The incremental displacement in the design parameter space introduced so that the constraint may be satisfied is taken in a direction normal to the constraint curve and is determined by the chord method in Eq. (20a). The incremental displacement given by Eq. (20b) is introduced along the constraint curve with the purpose of reducing the objective function. The sign of the increment is determined by comparing the values of the objective functions corresponding to the solution $\mathbf{W}^n_F$ and the perturbed solution $\mathbf{W}^n_{F,\varepsilon}$, which is defined below. The magnitude of the increment is increased by the factor $c_1(c_1 > 1)$ if two consecutive increments agree in sign, while it is reduced by the factor $c_2(c_2 < 1)$ if two consecutive increments differ in sign. Equations (20a) and (20b) are similar to the equations used in a previously developed optimization scheme.[9,11] However, the parameter τ defined in Eq. (22) differs from that used in the old scheme. We refer to the scheme presented here as scheme I, whereas we refer to the scheme of Refs. 9 and 11 as scheme II, which also shares some common elements with the scheme presented in Ref. 15.

The updated values of α'_F and $M'_{\infty F}$ are used to calculate the new flow iterative solution $\mathbf{W}^{n+1}_F$ by

$$\mathbf{W}^{n+1}_F = \psi(\mathbf{W}^n_F; \alpha'^{n+1}_F, M'^{n+1}_{\infty F}) \tag{24}$$

An additional perturbed solution $\mathbf{W}^{n+1}_{F,\varepsilon}$ is also calculated by

$$\mathbf{W}^{n+1}_{F,\varepsilon} = \psi(\mathbf{W}^n_{F,\varepsilon}; \alpha'^{n+1}_F, M'^{n+1}_{\infty F} + \varepsilon) \tag{25}$$

where ε is a small positive number. The perturbed solution, Eq. (25), is necessary for determining ΔE^n_M, as shown in Eq. (23). It also determines the angle of rotation θ^{n+1} of the α'_F and $M'_{\infty F}$ coordinate system relative to the α_F and $M_{\infty F}$ coordinate system. This angle is given by

$$\theta^{n+1} = \theta^n + \delta\theta^{n+1}$$

where the increment $\delta\theta^{n+1}$ is estimated by

$$\delta\theta^{n+1} = \tan^{-1}\{[L_F(\mathbf{W}^n_{F,\varepsilon}) - L_F(\mathbf{W}^n_F)]C_\alpha/\varepsilon\} \tag{26}$$

Although the optimization procedure is most suitably conducted in terms of the transformed parameters α'_F and $M'_{\infty F}$, the flow solution is calculated in terms of the physical parameters α_F and $M_{\infty F}$. These two sets of parameters are related by

$$\begin{bmatrix} \alpha^{n+1}_F \\ M^{n+1}_{\infty F} \end{bmatrix} = \begin{bmatrix} \cos\theta^{n+1} & -\sin\theta^{n+1} \\ \sin\theta^{n+1} & \cos\theta^{n+1} \end{bmatrix} \begin{bmatrix} \alpha'^{n+1}_F \\ M'^{n+1}_{\infty F} \end{bmatrix} \tag{27}$$

Angle-of-attack modifications are introduced by modifying the freestream flow direction, while Mach number modifications are introduced by updating the Mach numbers in the terms of the Euler equations shown in Eq. (1).

Results and Discussion

Several aspects of the correction procedure are investigated by applying it to a NACA 0012 airfoil tested in an open jet with zero pressure perturbations along the upper and lower boundaries. The airfoil is assumed to have a chord of unit length and to be located in the middle between the upper and lower boundaries. Two tunnel-height-to-chord ratios h are considered. They are $h = 3.6$ and $h = 4.6$. For the short tunnel ($h = 3.6$) computation, a 72×64 mesh is used for the tunnel simulation and a 72×96 mesh is used for the free-air simulation. For the high tunnel ($h = 4.6$) computation, a 72×80 mesh is used for the tunnel simulation and a 72×112 mesh is used for the free-air simulation. In all the following computations, the constraint formulation, which uses the η value defined by Eq. (11a), is used unless otherwise specified.

Comparison of Optimization Schemes

Scheme II was previously[9,11] used in wind-tunnel wall interference correction investigations. In these investigations, this scheme appeared to function properly. Comparisons between solutions at the model surface in the wind tunnel and in free air indicated that the corrections predicted produced free-air solutions that nearly match the wind-tunnel solutions as desired. A formal comparison, however, between the results predicted by scheme II and exact solutions was not performed. In previous computations in which scheme II was used, solutions with relatively small supersonic bubbles were investigated. In the present work, problems with higher freestream Mach numbers and higher angles of attack in comparison to those investigated in Ref. 11 are considered. It is found that, as the supersonic bubble size increases beyond a certain limit, scheme II does not converge. This is the main reason for developing the new optimization scheme, scheme I, presented here. A third scheme, termed here as scheme III, is introduced. This is a modification of scheme I in which the design parameter space is not rotated. The search for the minimum value of the objective function is conducted along constant α_F lines, as is done in scheme II. However, unlike scheme II where the choice of the incremental Mach number is based on information from two consecutive iterative solutions, scheme III, like scheme I, uses the perturbed solution, Eq. (25), in addition to the basic solution, Eq. (24), to determine the incremental Mach number. The three schemes are applied to a problem in which the airfoil is tested in an open jet of height $h = 3.6$. The airfoil lift coefficient and the tunnel Mach number are given by $L_e = 0.35$ and $M_{\infty e} = 0.7$.

In the first step of the correction procedure, the wind-tunnel flow is computed and the angle of attack α_T is determined. The initial iterative value of α_T is chosen to be given by $\alpha^0_T = 2.0$ deg, while the initial flowfield solution is set equal to freestream conditions. The parameters C_α and A_α in Eq. (17) are set equal to 0.3 and 0.2, respectively. In the second step of the correction procedure, the free-air flow is computed and

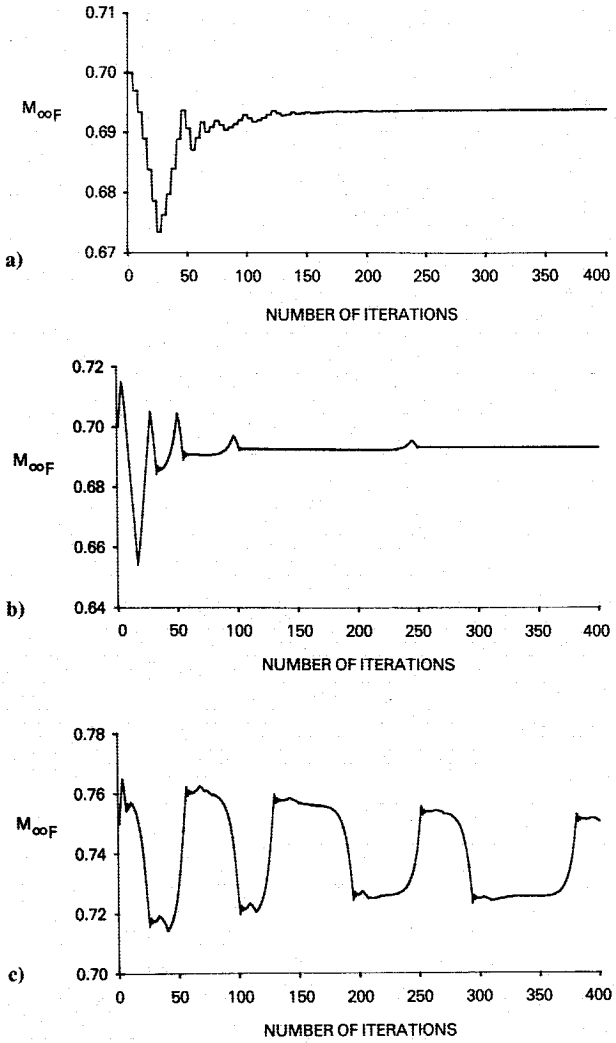

Fig. 1 Iterative history for $M_{\infty F}(h = 3.6,\ L_e = 0.35)$: a) scheme I, $M_{\infty e} = 0.7$; b) scheme II, $M_{\infty e} = 0.7$; and c) scheme II, $M_{\infty e} = 0.75$.

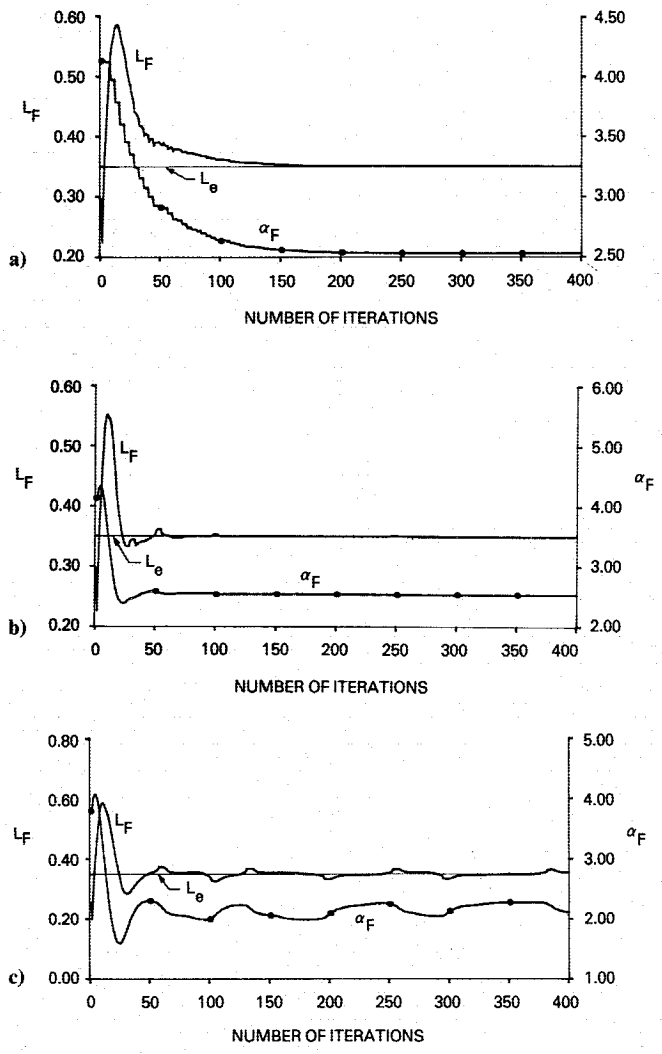

Fig. 2 Iterative histories for α_F and L_F $(h = 3.6,\ L_e = 0.35)$: a) scheme I, $M_{\infty e} = 0.7$; b) scheme II, $M_{\infty e} = 0.7$; and c) scheme II, $M_{\infty e} = 0.75$.

the parameters α_F and $M_{\infty F}$ are determined. The initial iterative values of α_F and $M_{\infty F}$ are chosen to be equal to α_T and $M_{\infty e}$, respectively. The initial flowfield solution is set equal to freestream conditions. The parameters $\delta M^0_{\infty F}$, c_1, c_2, C_α, A_α, ΔN, and ε are given, respectively, by 0.005, 1.2, 0.6, 0.3, 0.2, 4, and 10^{-5}. These values for the initial iterative solutions and the various scheme parameters are used in all the computations presented below.

The iterative history of $M_{\infty F}$ resulting from using scheme I is shown in Fig. 1a. In this figure, an initial stage of about 150 iterative steps is identified in which relatively rapid variations in the value of $M_{\infty F}$ take place. At the end of this stage, the value of $M_{\infty F}$ is essentially converged. Only minor variations are observed in the value of $M_{\infty F}$ beyond the initial stage. The iterative history of $M_{\infty F}$ resulting from using scheme II is shown in Fig. 1b. An initial stage of about 60 iterative steps of rapid variations is observed in this figure. The solution beyond this point seems to be essentially converged. However, at approximately the 80th and the 230th iterative steps, a rapid departure from the apparently converged solution takes place. Within about 25 iterative steps in both cases, an essentially converged solution is observed again. We have conducted many computations, using scheme II, for different test conditions. The appearance of local spike-shaped deviations is a common feature among these solutions. However, the size of these spikes and the frequency of their occurrence depend on the particular problem being solved. In scheme I, the incremental value $\delta M_{\infty F}$ is determined by comparing two objective functions at the same time step. In scheme II, this value is determined by comparing two objective functions at different time steps. Scheme II functions properly as long as the dependence of the objective function on the parameter $M_{\infty F}$ is stronger than its dependence on time. As its dependence on time becomes comparable or stronger than its dependence on $M_{\infty F}$, the computed $\delta M_{\infty F}$ values no longer lead to convergence to the optimum solution. The local divergence shown in Fig. 1b is due to the solution's weak dependence on $M_{\infty F}$ as the values of $\delta M_{\infty F}$ become small. As the local divergence occurs, the value of $\delta M_{\infty F}$ increases, causing a stronger dependence on $M_{\infty F}$ and causing reconvergence. In other words, the process that takes place at the spikes is self-stabilizing. It is, therefore, possible to use scheme II to determine a solution by simply ignoring the local solutions at the spikes. However, as the supersonic region increases in size, the size of the spikes also increases. Eventually, it becomes no longer possible to use scheme II for determining valid solutions. Figure 1c shows the iterative history of $M_{\infty F}$ resulting from using scheme II in the same problem solved above, but with a value of $M_{\infty e}$ of 0.75 rather than 0.7. It is apparent that a converged solution in this figure is no longer identifiable. Therefore, scheme II is no longer useful in determining a solution.

Figure 2 shows the iterative histories for the lift and angle of attack for the three cases corresponding to Fig. 1, while

Table 1 Comparison of the accuracy of the optimization schemes

	Exact	Scheme I	Scheme II	Scheme III
$\Delta\alpha$	−1.6000 deg	−1.5999 deg	−1.5981 deg	−1.6054 deg
ΔM	−0.0062	−0.0062	−0.0065	−0.0053
Error in $\Delta\alpha$	0.0%	0.0%	0.1%	−0.3%
Error in ΔM	0.0%	0.0%	−4.8%	14.5%
E_M	8.97×10^{-4}	8.97×10^{-4}	8.98×10^{-4}	9.09×10^{-4}
E_m	2.76×10^{-2}	2.76×10^{-2}	2.77×10^{-2}	2.74×10^{-2}

Fig. 3 shows the history for the maximum residual $R_{\max}$ for the same three cases. The effect of the spikes is seen to be local and limited to a few time steps in Fig. 2b. However, the recovery to the prespike level is seen to take a relatively longer time interval in the case of the maximum residual, as indicated in Fig. 3b. Figure 3b indicates that, beyond 300 time steps, the maximum residual oscillates about a fixed value. We have continued the computation to 800 time steps, and the oscillatory behavior was found to continue. This behavior is due to the same process that leads to the local divergence observed above. As indicated above, at certain stages of the computation, the signs and values of $\delta M_{\infty F}$ are no longer chosen in a manner that causes $M_{\infty F}$ to approach its optimum value. If conditions are such that the sign of $\delta M_{\infty F}$ remains unchanged for a large number of steps, then the local divergence observed above will occur. On the other hand, if the positive and negative signs of $\delta M_{\infty F}$ are reasonably well balanced, then the oscillatory behavior observed in Fig. 3b occurs. It should be noted that, even though the maximum residual may no longer converge, the level at which this occurs in Fig. 3b does indicate that, for practical purposes, the solution is converged. The uncertainty caused by scheme II in this particular problem should be of no practical concern. Scheme III was also used to solve the problem with an $M_{\infty e}$ value of 0.7. The resulting histories for $M_{\infty F}$, α_F, L_F, and $R_{\max}$, not shown here, were found to be very similar to those of scheme I (Figs. 1a, 2a, and 3a).

Table 1 compares the accuracy of the different schemes. The exact solution was obtained by solving a series of problems with different values of $M_{\infty F}$. In each problem the value of α_F, which satisfies the lift constraint, was determined by the chord method. In each of these problems, the objective function was computed. The exact solution is the solution that results in the minimum value for the objective function. The table includes a second measure of the residual wall interference effect E_m given by

$$E_m = \frac{\int |M_F - M_T| \, ds}{\int M_T \, ds}$$

This is a linear measure of the error and therefore may be more appropriate to use. The table indicates that scheme I is a highly accurate scheme. It also indicates that the results of scheme II are closer to those of scheme I than those of scheme III, contrary to our expectations. This is due to the uncertainty in determining the solutions of scheme II, which apparently resulted in a favorable deviation from scheme III. It does appear from the table, however, that the results obtained by each of the three schemes are accurate and any errors are within acceptable levels.

To compare the efficiency and relative costs of the different schemes, it is necessary to set a convergence criterion. The convergence criterion used here assumes that convergence is attained when $R_{\max} = 10^{-4}$. At this value of the maximum residual, it is found that the values of $\Delta\alpha$, ΔM, and E_M are all essentially converged. Based on this convergence criterion, Table 2 compares the number of iterations and the computational time required for convergence for the different schemes and for a regular analysis solution. It is clear from the table

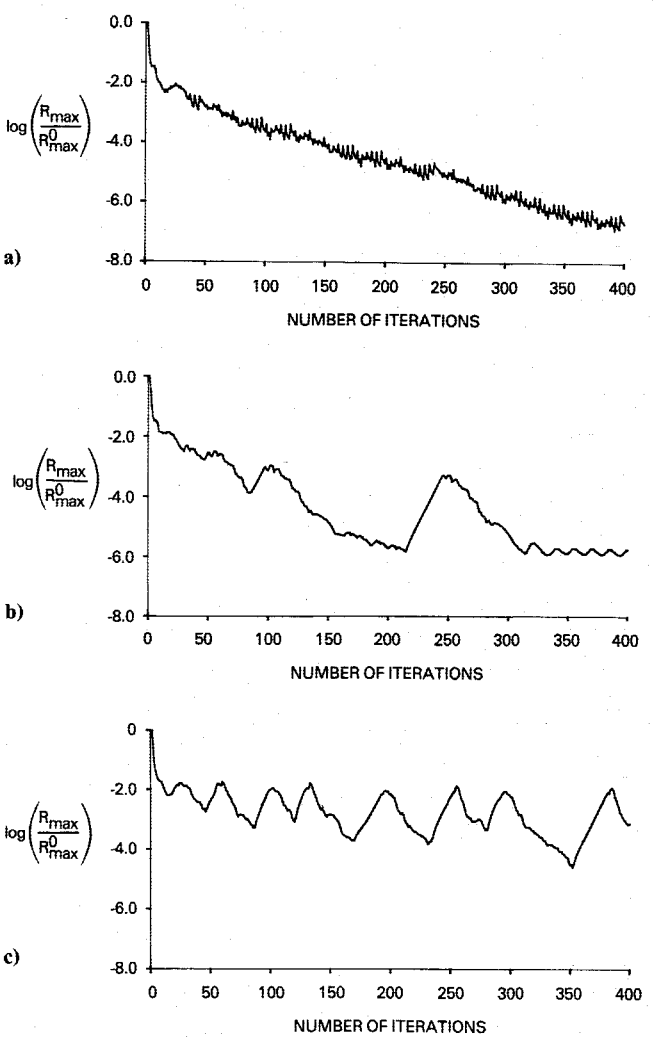

Fig. 3 Maximum residual evolution history ($h = 3.6$, $L_e = 0.35$): a) scheme I, $M_{\infty e} = 0.7$; b) scheme II, $M_{\infty e} = 0.7$; and c) scheme II, $M_{\infty e} = 0.75$.

that updating the angle of attack and the Mach number in addition to the flow variables results in reduced convergence rates relative to that of an analysis problem in which only the flow variables are updated. The table also indicates that the computational time per iteration required for scheme I is double that of scheme II. This is due to the requirement of computing two solutions in parallel when scheme I is used. Although scheme II updates α_F and $M_{\infty F}$ for each iterative step, scheme I, through the parameter ΔN, allows the user to specify the frequency of updating these parameters. In the present computations, these parameters were updated every four iterative steps. We did not attempt to determine the value of ΔN that maximizes the rate of convergence. Therefore, there is a good possibility that the efficiency of scheme I can be improved over that indicated.

Table 2 Comparison of the efficiency of the optimization schemes

	Analysis	Scheme I	Scheme II	Scheme III
Number of iterations	92	268	174	262
CPU seconds	23	137	44	134

The above computations were performed for a case in which scheme II functions properly to allow comparison between that scheme and the other schemes in the range in which it is valid. In the following computations, we investigate problems at higher Mach numbers. Scheme II cannot be used in that range. We, therefore, limit ourselves to the use of scheme I.

Verification of Wind-Tunnel Boundary Conditions

Both the wind-tunnel and the free-air outer boundary conditions were derived using the Riemann invariants for a one-dimensional flow. The error introduced by this formulation is expected to affect the flow solution near the airfoil. This effect, however, is expected to be stronger in the case of the wind-tunnel simulation for which the boundary conditions are applied in the near field, than in the case of the free-air simulation, for which the boundary conditions are applied in the far field. The objective of the following computation is to verify that the errors introduced by applying the present tunnel boundary conditions do not exceed acceptable levels.

In the following example, the measured tunnel pressure data are replaced by numerical solutions of the Euler equations simulating free-air flow conditions. In other words, an interference-free tunnel is assumed. The exact solution for this example is known. It is given by $\Delta\alpha = \Delta M = 0$. The test conditions are given by $\alpha_e = 1.8$ deg, $M_{\infty e} = 0.78$, $L_e = 0.3552$, and $h = 4.6$. In the first step of the correction procedure, the angle of attack is determined to be given by $\alpha_T = 1.8022$ deg. The deviation of this value from the exact value is 0.0022 deg. This deviation is due to the approximations introduced in the tunnel boundary conditions. In the second step of the correction procedure, the parameters α_F and $M_{\infty F}$ are determined. They are given by $\alpha_F = 1.8010$ deg and $M_{\infty F} = 0.7799$. The corrections $\Delta\alpha$ and ΔM are, therefore, given by $\Delta\alpha = -0.0012$ deg and $\Delta M = -0.0001$. Although not identically zero, the errors in determining $\Delta\alpha$ and ΔM are acceptably small. This indicates that the present formulation of the tunnel boundary conditions is adequate.

Effects of Varying the Test Parameters

The effects of varying the test parameters h, $M_{\infty e}$, and L_e on the correction results $\Delta\alpha$, ΔM, and E_M are investigated by introducing perturbations to these parameters from base test conditions defined by $h = 4.6$, $M_{\infty e} = 0.8$, and $L_e = 0.35$. Before studying these effects, details of the base calculation are first presented.

Figure 4 shows the iterative histories for α_T, L_T, and $R_{\max}$ in the first step of the correction procedure for the problem defined by the base test conditions. The first step of the correction procedure determines an α_T value of 2.896 deg. Ninety-eight iterations and 23 CPU seconds were required for convergence in this step. Figure 5 shows the iterative histories for $M_{\infty F}$, α_F, L_F, and $R_{\max}$ in the second step of the correction procedure. This step determines an α_F value of 1.6488 deg and an $M_{\infty F}$ value of 0.7871. A comparison between the solution obtained in the second step and a regular analysis solution indicates that 246 iterations and 143 CPU seconds are required for the present solution to achieve convergence, while 66 iterations and 19 CPU seconds are required for the analysis solution to achieve convergence. The correction results are

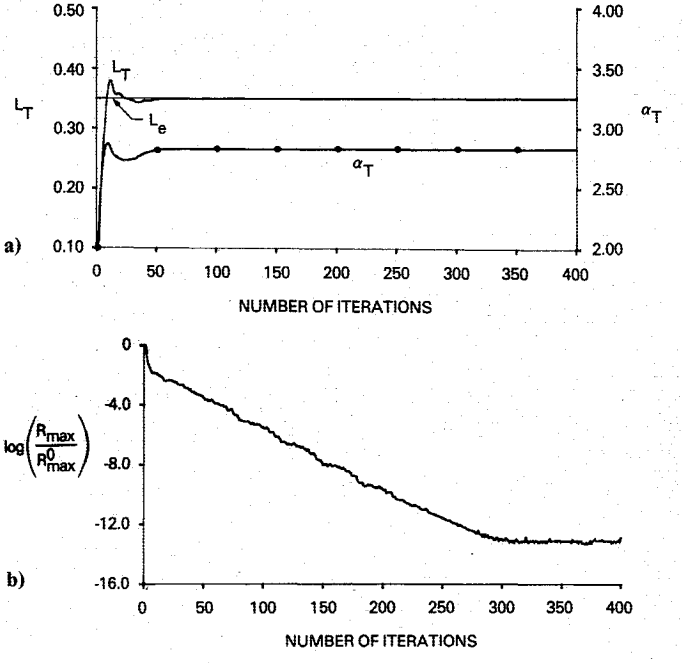

Fig. 4 Iterative histories for the wind-tunnel solutions ($h = 4.6$, $M_{\infty e} = 0.8$, $L_e = 0.35$): a) α_T and L_T; and b) maximum residual.

given by

$$\Delta\alpha = -1.1808, \quad \Delta M = -0.0129, \quad E_M = 3.54 \times 10^{-4} \tag{28}$$

These values are identical to the exact solution. Figure 6 presents a comparison between the pressure on the airfoil surface for the wind-tunnel flow ($M_{\infty T} = 0.8$, $\alpha_T = 2.8296$ deg), the free-air flow at the uncorrected conditions ($M_{\infty F} = 0.8$, $\alpha_F = 2.8296$ deg), and the free-air flow at the corrected conditions ($M_{\infty F} = 0.7871$, $\alpha_F = 1.6488$ deg). As indicated from the figure, the correction procedure does accomplish the goal of determining the free-air corrected conditions α_F and $M_{\infty F}$ with aerodynamic properties nearly matching the corresponding properties for the tunnel conditions α_T and $M_{\infty T}$. The value of E_M is reduced from 384.36×10^{-4} for the free-air flow at the uncorrected conditions to 3.54×10^{-4} for the free-air flow at the corrected conditions.

The same problem was solved using the definition given by Eq. (11b) for η instead of that given by Eq. (11a). Two-hundred and fifty-seven iterations and 149 CPU seconds were required for convergence. The correction results in this case are

$$\Delta\alpha = -1.1350, \quad \Delta M = -0.0135, \quad E_M = 3.07 \times 10^{-4} \tag{29}$$

The improvement seen in these results over those given above, Eq. (28), is evident by the smaller value of E_M in Eq. (29). However, the error caused by using the definition of Eq. (11a) for η instead of definition of Eq. (11b) is apparently small.

The results of varying the test parameters h, $M_{\infty e}$, and L_e are presented in Table 3. The results presented in the table are

Table 3 Effect of test conditions on the residual interference

h	$M_{\infty e}$	L_e	α_T	$\Delta\alpha$	ΔM	E_M	E_m
4.6	0.80	0.35	2.8296	−1.1808	−0.0129	3.54×10^{-4}	1.90×10^{-2}
3.6	0.80	0.35	3.3825	−1.6917	−0.0191	8.80×10^{-4}	2.99×10^{-2}
4.6	0.85	0.35	2.3907	−1.2552	−0.0198	17.69×10^{-4}	3.05×10^{-2}
4.6	0.80	0.40	3.2628	−1.3401	−0.0145	4.66×10^{-4}	2.18×10^{-2}
3.6	0.85	0.40	3.4226	−2.0157	−0.0311	34.50×10^{-4}	4.73×10^{-2}

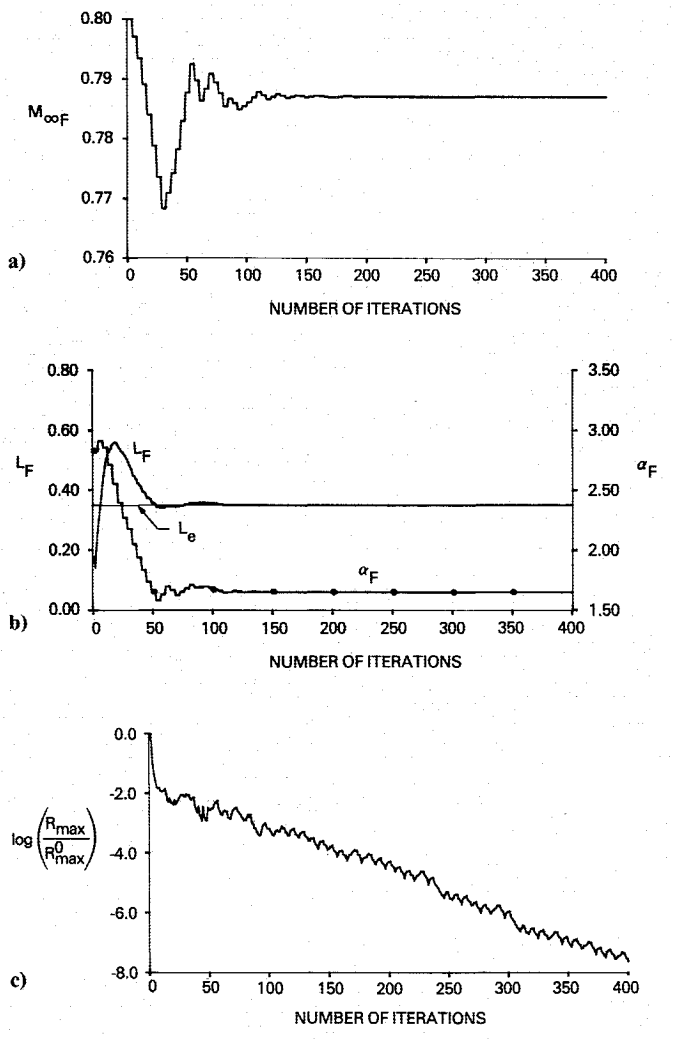

Fig. 5 Iterative histories for the free-air solutions ($h = 4.6$, $M_{\infty e} = 0.8$, $L_e = 0.35$): a) $M_{\infty F}$; b) α_F and L_F; and c) maximum residual.

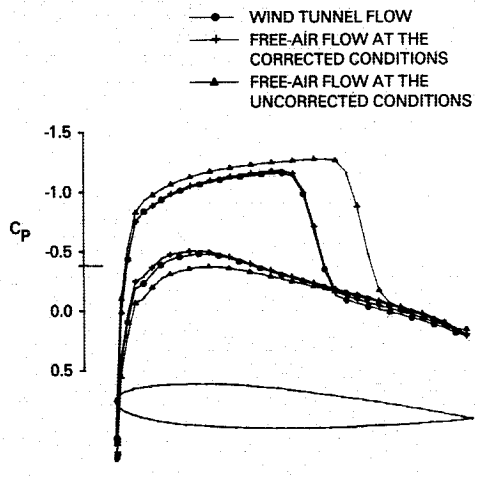

Fig. 6 Pressure distribution on the airfoil surface ($h = 4.6$, $M_{\infty e} = 0.8$, $L_e = 0.35$).

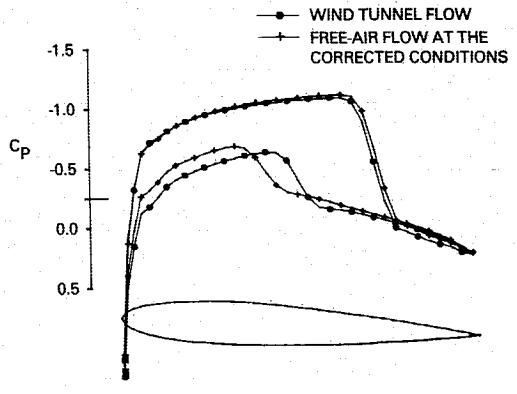

Fig. 7 Pressure distribution on the airfoil surface ($h = 3.6$, $M_{\infty e} = 0.85$, $L_e = 0.4$).

computed using the formulation of Eq. (11a). The table indicates that the effects of reducing h, increasing $M_{\infty e}$, or increasing L_e is to increase the magnitude of the corrections $\Delta\alpha$ and ΔM, indicating an increase in wall interference effects. Associated with this increase is an increase in the residual wall interference, as indicated by the values of E_M and E_m, indicating a reduced quality in the test data. A comparison between the free-air flow solution at the corrected conditions and the tunnel solution is given in Fig. 6 for the base test case with the least wall interference effects and the smallest residual wall interference effect. Figure 7 compares the free-air flow solution at the corrected conditions and the tunnel solution for the case in which all the test conditions are perturbed. This is the case with the most wall interference effects and the largest residual wall interference effect. As expected, the deviation between the wind-tunnel solution and the free-air solution at the corrected conditions is greater in Fig. 7 than in Fig. 6. Reducing h, increasing $M_{\infty e}$, or increasing L_e further will lead to greater deviations between the two solutions. At a certain stage, these deviations exceed the acceptable level. Therefore, when correcting experimental data it is necessary to define a value for E_M or E_m as an upper limit for acceptable data.

The cases presented in Table 3 were recomputed using Eq. (11b) for η. The difference between the recomputed results and those given in the table were confined to a range given by 3–7%, 4–6%, 13–16%, and 2–9% for $\Delta\alpha$, ΔM, E_M, and E_m, respectively. The effect of Eq. (11b) is to reduce the magnitude of $\Delta\alpha$ and increase the magnitude of ΔM. Although each of the solutions converged to at least a three-decimal-place accuracy in the values of $\Delta\alpha$ and ΔM, convergence in some of the cases did not continue beyond this point. This is apparently an optimization problem introduced by making the constraint a stronger function of $M_{\infty F}$. This unfavorable effect on the optimization scheme may be remedied by fixing the value of η in Eq. (9b) for a number of iterations and only updating it periodically.

Further Comments

All of the above computations have been performed using a single set of values for the computational parameters c_1, c_2, C_α, A_α, ΔN, and ε. The effect of varying these parameters on the convergence properties of the schemes used was not investigated, although it may increase computational efficiency. It is worth noting that problems associated with scheme II as the Mach number increases and those associated with scheme I at high Mach numbers, in the case of normalizing the lift by the total pressure, might be resolved by choosing different values for the computational parameters.

The main computational costs are due to the free-air simulation (step 2) and not to the tunnel simulation (step 1). Scheme I requires that two flowfield computations be performed in step 2, whereas only a single computation is required in step 1. In the computations performed here, the free-air computational mesh was chosen to coincide with the tunnel mesh in their overlapping region. Although the meshes are required to coincide near the airfoil surface, they are not required to coincide throughout the tunnel region. Therefore, it is possible to reduce the computational costs by reducing the number of horizontal mesh lines in the free-air computation. The benefit of not having totally overlapping meshes in the wind-tunnel region becomes even greater in three-dimensional calculations, since this idea is applicable there in both the vertical and spanwise directions.

Transonic wall interference correction procedures are relatively complex. Three different aspects may be identified in these procedures. The main focus of this study has been on the numerical aspect of the problem. Certain effects, such as the sidewall boundary-layer effects,[16] have been previously investigated and are not included in the present formulation. However, it may be modified to include them. The second aspect of the correction procedure is the experimental aspect, which requires that pressure measurements be made near the wind-tunnel wall to supply the required boundary conditions for the correction procedure. The task of making enough measurements in the wind tunnel to supply the boundary conditions at the boundary points of a relatively fine computational mesh is not an easy one. This is particularly true in three-dimensional tests. The final element of the correction procedure attempts to estimate the numerical boundary conditions from experimental measurements through aerodynamic interpolation.[17] Different modifications may be introduced to the correction scheme presented here that affect its accuracy, complexity, and computational requirements. Some of these variations were presented in the present investigation. It is, however, important to note that the level of accuracy of the results computed by the scheme are dependent on the levels of accuracy employed in all three aspects of the correction procedure. It is therefore desirable to have a uniform level of accuracy in all three aspects of the correction procedure.

Conclusions

The main elements of a transonic wind-tunnel wall interference correction procedure have been developed and tested. In the procedure, the corrected Mach number and angle of attack are those optimum values that minimize the Mach number difference on the model surface in the tunnel and in free air while matching the lift. An estimate of the correctability of the data, by varying the Mach number and the angle of attack, is provided by the procedure. Although the procedure is developed and tested for two-dimensional problems, its basic elements are extendable to three-dimensional problems.

Through perturbing test conditions, the effects of tunnel height, freestream Mach number, and airfoil lift on wall interference and residual wall interference were investigated. Two formulations for the lift constraint were considered. The formulation based on normalizing the lift by the freestream total pressure is the more accurate, since it removes the freestream Mach number dependence from the expression for the normalized lift. There are indications that the relatively strong dependence of the constraint function in this case on the freestream Mach number may lead to difficulties in solution convergence. Methods to avoid these problems were suggested. The formulation based on using the regular lift coefficient is an approximation due to its explicit dependence on the freestream Mach number. However, it is a valid approximation since Mach number corrections are generally small. As the Mach number correction becomes large, this is an indication of the uncorrectability of the data. It is in this situation that the accuracy of this formulation deteriorates.

The tests conducted here indicate that optimization scheme I, developed in the present work, is highly reliable and accurate. A second scheme previously developed, and referred to here as scheme II, is found to be useful only for a certain range of test conditions for which a relatively small supersonic region is present in the flowfield. Although scheme II determines approximate solutions to the optimization problem, the results obtained here are in agreement with previous results in indicating that the accuracy of the solutions predicted by that scheme are generally acceptable. Under those conditions for which scheme II is applicable, it has the advantages of higher efficiency and less memory requirements in comparison to scheme I. The use of scheme II may be most advantageous in solving three-dimensional problems, in view of the high cost of computations and the large computer-memory requirements associated with these problems.

The optimization scheme developed here is based on updating the iterative solutions for the flow variables and the design parameters simultaneously. Although applied here to a two-design parameter problem, it may be extended to solve general aerodynamic design problems.

Acknowledgments

This work was sponsored by NASA Ames Research Center under Contract No. NAS2-12157.

References

[1]Garner, H. C., Rogers, E. W. E., Acum, W. E. A., and Maskell, E. C., "Subsonic Wind-Tunnel Wall Corrections," AGARDograph 109, Oct. 1966.

[2]Capelier, C., Chevallier, J. P., and Bouniol, F., "Nouvelle Methode de Correction des Effects de Parois en Courant Plan," *La Recherche Aerospatiale*, Jan.–Feb. 1978, pp. 1–11.

[3]Schairer, E. T., "Two-Dimensional Wind-Tunnel Interference from Measurements on Two Contours," *Journal of Aircraft*, Vol. 21, June 1984, pp. 414–419.

[4]Kraft, E. M. and Dahm, W. J. A., "Direct Assessment of Wall Interference in a Two-Dimensional Subsonic Wind Tunnel," AIAA Paper 82–0187, Jan. 1982.

[5]Mokry, M., Chan, Y. Y., and Jones, D. J., "Two-Dimensional Wind-Tunnel Wall Interference," AGARDograph 281, Nov. 1983.

[6]Kemp, W. B., Jr., "Toward the Correctable-Interference Transonic Wind Tunnel," Proceedings of the AIAA 9th Aerodynamic Testing Conference, June 1976, pp. 31–38.

[7]Kemp, W. B., Jr., "Transonic Assessment of Two-Dimensional Wind-Tunnel Wall Interference Using Measured Wall Pressures," NASA CP-2045, March 1978, pp. 473–486.

[8]Murman, E. M., "A Correction Method for Transonic Wind-Tunnel Wall Interference," AIAA Paper 79–1533, July 1979.

[9]Rizk, M. H. and Murman, E. M., "Wind-Tunnel Wall Interference Corrections for Aircraft Models in the Transonic Regime," *Journal of Aircraft*, Vol. 21, Jan. 1984, pp. 54–61.

[10]Jameson, A. and Baker, T. J., "Solution of the Euler Equations for Complex Configurations," AIAA Paper 83–1929, July 1983.

[11]Rizk, M. H. and Lovell, D. R., "Two-Dimensional Transonic Wind-Tunnel Wall Interference Corrections Based on the Euler Equations," AIAA Paper 86–0124, Jan. 1986.

[12]Jameson, A. and Baker, T. J., "Multigrid Solution of the Euler Equations for Aircraft Configurations," AIAA Paper 84–0093, Jan. 1984.

[13]Jameson, A., Schmidt, W., and Turkel, E., "Numerical Solutions of the Euler Equations by Finite-Volume Methods Using Runge-Kutta Time-Stepping Schemes," AIAA Paper 81-1259, June 1981.

[14]Pelz, R. and Steinhoff, J., "Multigrid ADI Solutions of the Transonic Full Potential Equation for Airfoils Mapped to Slits," *Symposium on Computers in Flow Prediction and Fluid Dynamics Experiments,* American Society of Mechanical Engineers Winter Meeting, Washington, DC, Nov. 1981, p. 27.

[15]Kemp, W. B., Jr., "TWINTN4: A Program for Transonic Four-Wall Interference Assessment in Two-Dimensional Wind Tunnels," NASA CR-3777, Feb. 1984.

[16]Sewall, W. G., "Effects of Sidewall Boundary Layers in Two-Dimensional Subsonic and Transonic Wind Tunnels," *AIAA Journal,* Vol. 20, Sept. 1982, pp. 1253-1256.

[17]Kemp, W. B., Jr., "A Slotted Test Section Numerical Model for Interference Assessment," AIAA Paper 84-0627, March 1984.